Journal of Physics: Energy

OPEN ACCESS

RECEIVED
30 January 2020

REVISED
7 April 2020

ACCEPTED FOR PUBLICATION
21 April 2020

PUBLISHED
14 July 2020

Original content from this work may be used under the terms of the Creative Commons Attribution 4.0 licence. Any further distribution of this work must maintain attribution to the author(s) and the title of the work, journal citation and DOI.

Topical Review

Review of $ZnSnN_2$ semiconductor material

Imran S. Khan[1], **Karen N. Heinselman**[1] and **Andriy Zakutayev**[2]

National Renewable Energy Laboratory, Golden, Colorado 80401, United States of America

E-mail: andriy.zakutayev@nrel.gov

Keywords: nitride, photovoltaic, sputtering, density functional theory, disorder, doping, band gap

Supplementary material for this article is available online

Abstract

Zinc tin nitride ($ZnSnN_2$) is one of the emerging ternary nitride semiconductors considered for photovoltaic device applications due to its attractive and tunable material properties and earth abundance of constituent elements. Computational predictions of the material properties sparked experimental synthesis efforts, and currently there are a number of groups involved in $ZnSnN_2$ research. In this article, we review the progress of research and development efforts in $ZnSnN_2$ across the globe, and provide several highlights of accomplishments at the National Renewable Energy Laboratory (NREL). The interplay between computational predictions and experimental observations is discussed and exemplified by focusing on unintentional oxygen incorporation and the resulting changes in optical and electronic properties. The research progress over the past decade is summarized, and important future development directions are highlighted.

1. Introduction

Nitride semiconductors are a promising class of materials for a wide variety of energy conversion and electronic device applications because of their intermediate bonding character compared to ionic compounds (e.g. oxides, fluorides) and covalent materials (e.g. sulfides, phosphides) [1, 2]. The degree of ionic character in nitrides provides a greater tolerance to structural defects due to atomic orbitals proximity to the band edges and the partially covalent character. This is due to the high energy of the nitrogen 2p orbital which provides better hybridization with metal orbitals, leading to lower bandgaps, improved charge transport properties, and easier p-type doping [3, 4]. It is also interesting that nitrides are relatively underexplored compared to many other materials' families: there are over an order of magnitude more oxides than nitrides in crystallographic databases [5, 6]. The lower energy of the N_2 compared to O_2 molecule causes the apparently less stable character of nitrides, but after breaking the N_2 triple bond, nitrides are just as stable as oxides as evidenced by their applications in hard and refractory coatings [7, 8]. Nevertheless, due to the stability of the N_2 molecule and the favorable nature of oxide formation, nitrides are typically quite difficult to synthesize, especially in bulk form from molecular N_2 precursor. The main ways to incorporate more reactive nitrogen into a growth are high pressure synthesis [9, 10]; thermal cracking of ammonia NH_3 [11, 12]; sacrificial solid state azide precursors such as NaN_3, also leading to Na flux [13, 14]; and RF or microwave frequency plasma of nitrogen N_2 [15, 16].

Binary III–V nitrides such as GaN, AlN, InN and their alloys with wurtzite crystal structures have already revolutionized optoelectronic, electronic, and electromechanical technologies, including (In,Ga)N light emitting diodes (LEDs) in solid state lighting [18, 19], (Al,Ga)N radio-frequency (RF) transistors in military applications [20, 21], and (Al,Sc)N piezoelectric resonator microelectromechanical systems (MEMS) in telecommunications [22, 23]. All these transformative results were largely dependent on the use of chemical alloying to facilitate tuning of band offsets and other materials properties, and growth of epitaxial heterostructures to improve materials quality and enable spatial variations in electronic structure [24–26].

[1] These authors equally contributed to this paper
[2] Author to whom any correspondence should be addressed.

© 2020 The Author(s). Published by IOP Publishing Ltd

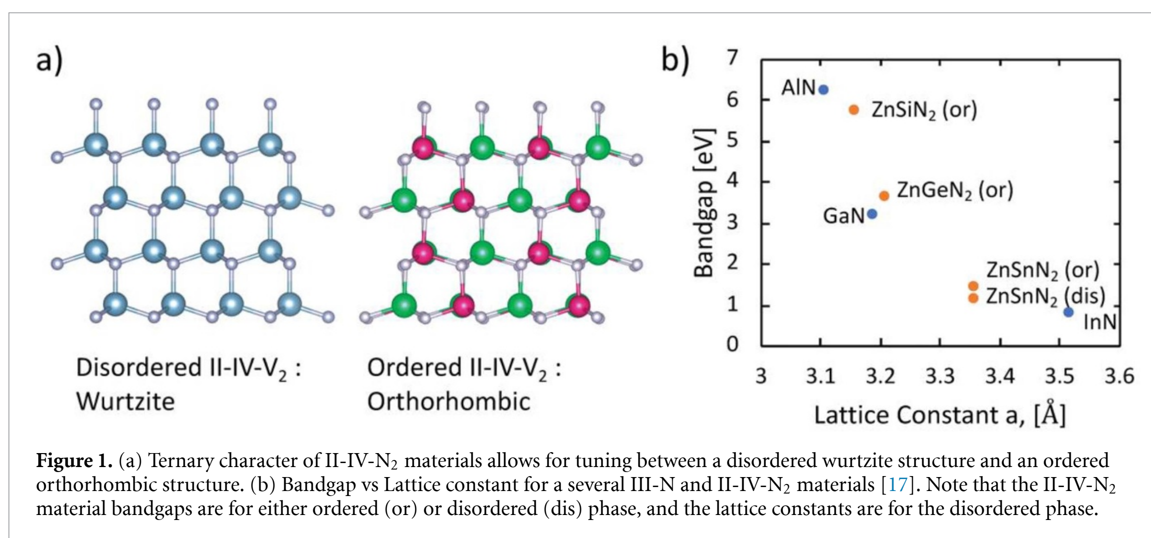

Figure 1. (a) Ternary character of II-IV-N_2 materials allows for tuning between a disordered wurtzite structure and an ordered orthorhombic structure. (b) Bandgap vs Lattice constant for a several III-N and II-IV-N_2 materials [17]. Note that the II-IV-N_2 material bandgaps are for either ordered (or) or disordered (dis) phase, and the lattice constants are for the disordered phase.

III-Nitride materials have also opened the door to novel photovoltaic and photoelectrochemical applications, beyond the well-known case of 'dilute nitrides' [27, 28]. Using metalorganic chemical vapor deposition (MOCVD) to grow InGaN multiple quantum well (MQW) structures has opened up a pathway to high efficiency solar cells at high temperatures of up to 600 °C, of particular interest for integration with concentrated solar power (CSP) systems and space applications [29, 30]. GaN and InGaN nanowire photoelectrodes have also been reported to exhibit hydrogen generation by photoelectrochemical water splitting with high efficiency and stability [31–33].

Ternary wurtzite-derived II-IV-N_2 nitrides, such as $ZnSnN_2$ $ZnGeN_2$ $ZnSiN_2$, can be thought of as analogues to the wurtzite III-N nitrides, with the unit cell doubled and two group-III elements replaced by a group-II and a group-IV element [17]. The resulting hexagonal wurtzite-derived structure may also have II/IV cation ordering, which leads to a lower-symmetry orthorhombic unit cell (figure 1(a)) and adds a tuning parameter for bandgap and effective mass based on degree of cation disorder while maintaining stoichiometry and lattice constant (figure 1(b)). As a result, Zn(Sn, Ge, Si)N_2 materials have a wide range of bandgap tuning, ranging from >5 eV to ~1 eV, spanning the visible spectrum and extending into the IR and UV. A transition from binary III–V towards ternary II-IV-N_2 chemistry also enables doping control through the combination of off-stoichiometry and compensating defects. Among all these III–V and II-IV-N_2 materials, $ZnSnN_2$ (ZTN) is one of the most attractive candidates for photovoltaic (PV) solar cell applications, due to large abundance of the elemental sources [34] and the solar-matched bandgap [35].

This article reviews the progress and challenges in research and development of $ZnSnN_2$ materials and applications. First, we outline a history of $ZnSnN_2$ investigations around the world, as published in peer reviewed literature. Second, we highlight a few recent accomplishments in $ZnSnN_2$ research by our team at National Renewable Energy Laboratory (NREL), with the focus on understanding and controlling $ZnSnN_2$ structure and properties. Finally, we briefly summarize this research and highlight important next steps necessary to advance $ZnSnN_2$ materials and devices. In summary, we conclude that although $ZnSnN_2$ device development has seen only limited success so far, significant progress has been made in $ZnSnN_2$ materials research, which should enable improved devices in the near future.

2. Brief history of $ZnSnN_2$ research

In this section, we briefly summarize the history of research on $ZnSnN_2$ published in literature. Highlights include both computational and experimental studies of synthesis, structure, optical and electrical properties, as well as $ZnSnN_2$ containing photovoltaic devices. A summary of key milestones in $ZnSnN_2$ research for each of these topics is presented in figure 2, with corresponding references listed in supplemental table S1.

2.1. Computational studies

Research interest in $ZnSnN_2$ was started by the computational modelling of the Zn-IV-N_2 compounds in 2008 [39, 40]. Using Density Functional Theory (DFT) with Local Density Approximation (LDA), physical properties such as phonon density, band dispersions, specific heat, lattice constant, dielectric constants, elasticity and polarization properties were calculated. Follow-up publications from the same group further investigated the band structure and electronic properties and reported a computed bandgap of 1.65 eV for ZTN [41], which was later revised to 2.02 eV [42]. Further research focused on the computed band

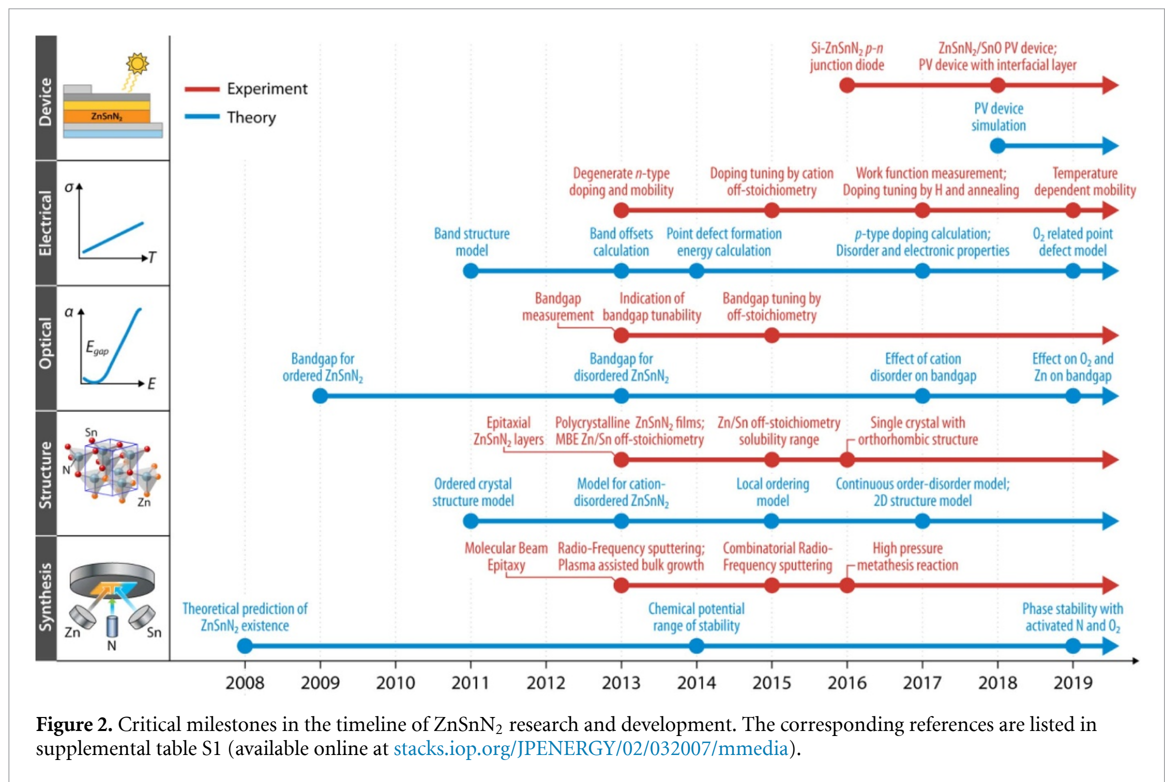

Figure 2. Critical milestones in the timeline of $ZnSnN_2$ research and development. The corresponding references are listed in supplemental table S1 (available online at stacks.iop.org/JPENERGY/02/032007/mmedia).

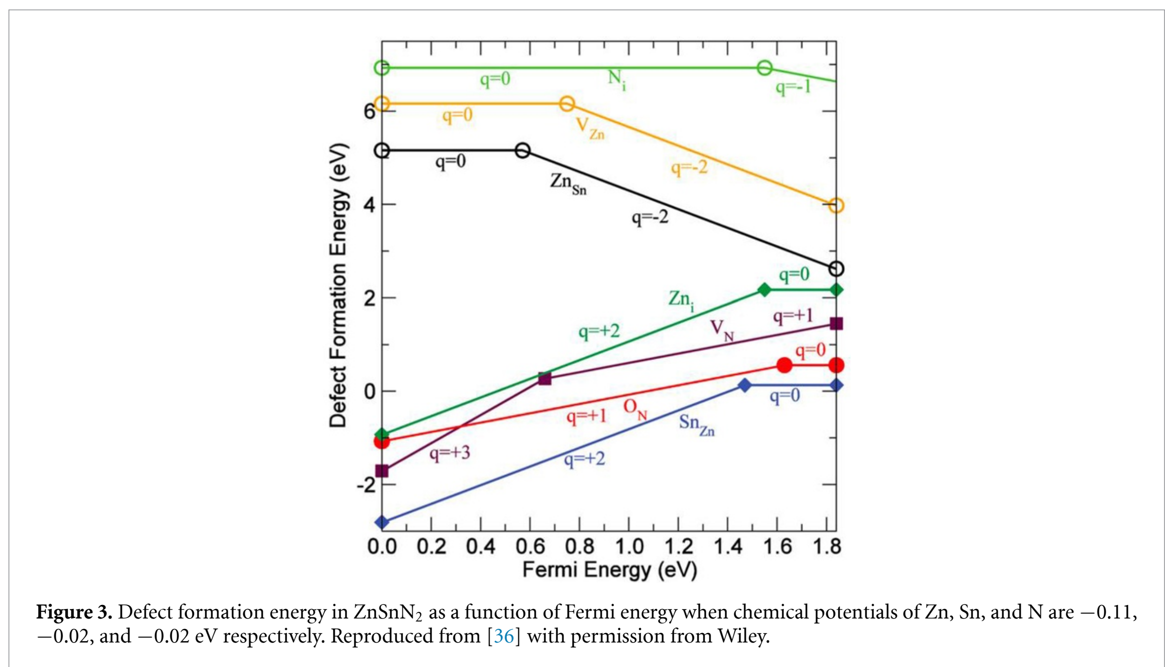

Figure 3. Defect formation energy in $ZnSnN_2$ as a function of Fermi energy when chemical potentials of Zn, Sn, and N are −0.11, −0.02, and −0.02 eV respectively. Reproduced from [36] with permission from Wiley.

alignment of ZTN with ZnO and GaN and a type II band alignment was reported, suggesting potential solar cell application [43].

With time, first principles modelling evolved, taking into account the results from experimental findings. Early analyses assumed there is a fully 'ordered' or a fully 'disordered' crystal structure, which could not explain the apparent lattice disorder deduced from x-ray diffraction spectra and the insensitivity of the bandgap to such apparent disorder. Fully ordered $ZnSnN_2$ is kinetically unfavorable, and the octet-rule-violating fully random structures are energetically very costly. A significant achievement of the computational studies was the explanation of disorder as mixing of two different octet-rule preserving charge-neutral crystal structures ($Pna2_1$ and $Pmc2_1$ phases) [44]. Fully 'random-like' XRD was explained with random stacking of the two structures, while properties like bandgap was defined by local disorder.

Phase stability and defect distribution (figure 3) of ZTN based on first principle calculations were presented [36], indicating that Sn_{Zn} antisites are the dominant donor defect, along with possible deep O_N

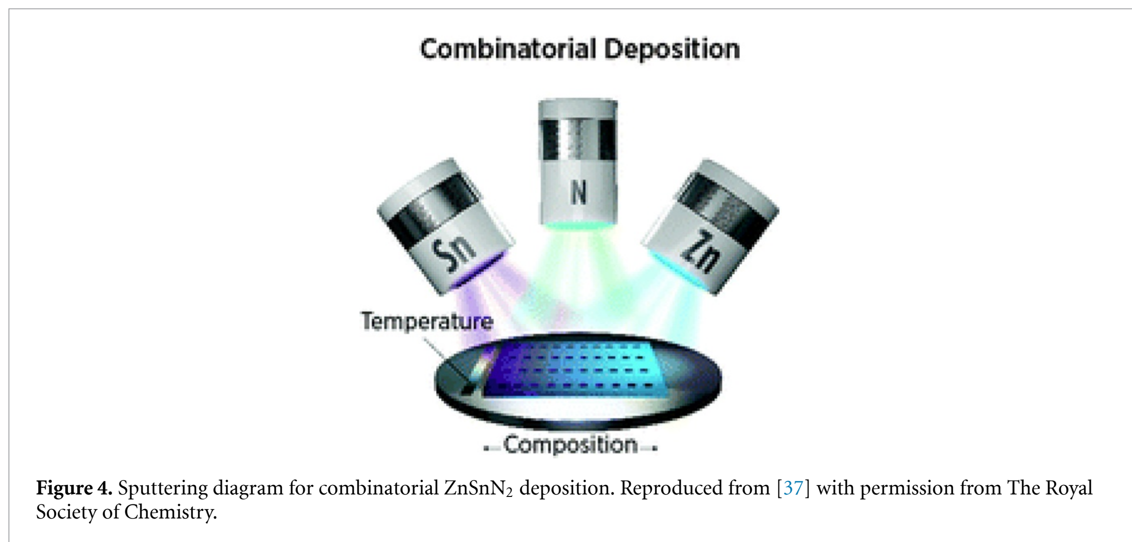

Figure 4. Sputtering diagram for combinatorial $ZnSnN_2$ deposition. Reproduced from [37] with permission from The Royal Society of Chemistry.

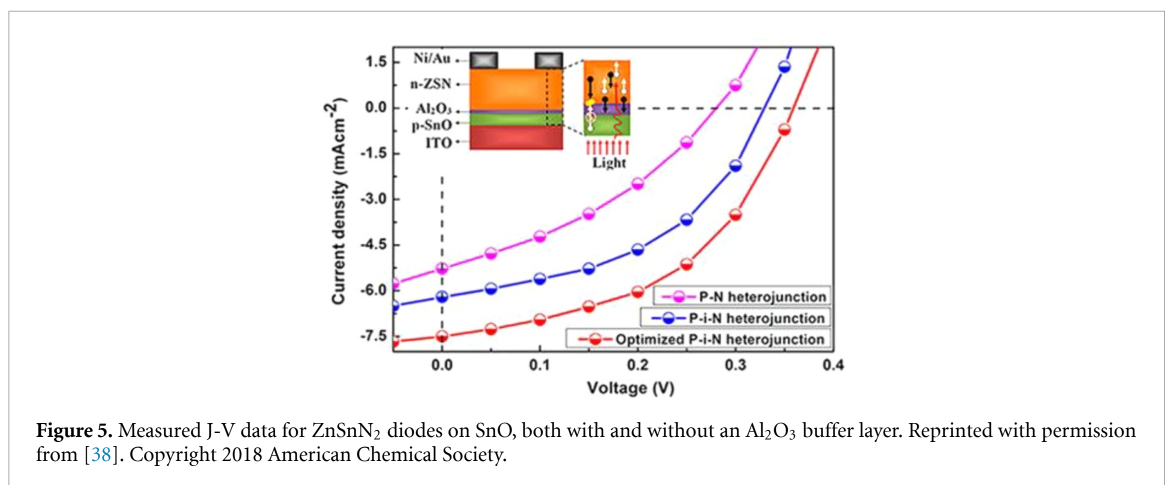

Figure 5. Measured J-V data for $ZnSnN_2$ diodes on SnO, both with and without an Al_2O_3 buffer layer. Reprinted with permission from [38]. Copyright 2018 American Chemical Society.

impurities. However, based on updated calculations of the point defects, the calculations predicted no deep (intrinsic) defects in the structure of ZTN [45]. The p-type dopability of ZTN with Li, Na and K was investigated computationally, and Li_{Zn} was identified as a potential shallow acceptor [46]. Recently these point defect models have been further revised and refined [47, 48], taking into account effects of cation disorder and off-stoichiometry that are often observed in experimental literature. Alternative structures of ZTN were also computationally predicted, such as ZTN/ZnO short-period superlattices [49] and 2D ZTN [50], and potential for photocatalytic applications of the latter was suggested. However, no reports of experimental synthesis of the 2D or superlattice structures have been published to date.

2.2. Experimental studies

Experimental synthesis of $ZnSnN_2$ was achieved in 2013 by three independent research groups, using radio-frequency (RF) sputtering [51], molecular beam epitaxy (MBE) [52], and plasma-assisted vapor–liquid–solid (PVLS) growth [53]. A follow-up study explored the region of temperature and Zn:Sn composition for high quality ZTN growth [54]. MBE was used to grow ZTN epitaxially on Yttria-stabilized Zircona (YSZ) substrates [52], and it was predicted that the bandgap of ZTN is tunable between 1.0 and 2.0 eV, based on the level of cation disorder in the films [55]. Zn/Sn off-stoichiometry in MBE growth was later investigated, with claims that the resulting films exhibit a monoclinic structure, indicative of cation disorder [56]. The first reported reportedly orthorhombic ZTN was grown by MBE on $LiGaO_2$ substrates [57]. PMBE was used to grow non-polar single crystal $ZnSnN_2$ with pseudo-wurtzite [11–20] orientation on sapphire substrate with ZnO buffer layer [58].

The first ZTN growth by RF sputtering used sapphire and GaN as substrates [51]. The structure was found to be wurtzite-derived and reported orthorhombic, and a high degenerate doping concentration of 10^{21} cm^{-3} was identified. Discrepancy between the measured optical bandgap of 2 eV and the calculated direct bandgap of 1.42 eV was explained by conduction band filling due to the Burstein-Moss effect. The work function and valence band position were measured in a follow up study [59], and it was concluded that

surface states due to ambient oxygen exposure caused band bending, shifting the Fermi level towards mid-gap. Highly crystalline ZTN thin films were studied for chemical environments of the constituent elements using XPS and Mössbauer spectrometry, and an ambient oxygen contamination mechanism through the grain boundary was proposed [60]. Piezotronic and piezophototronic properties of combinatorial RF sputter deposited $ZnSnN_2$ have also been studied [61].

Several other reports of ZTN growth by RF sputtering have been published. Doping control has been achieved by Zn-rich off-stoichiometry using combinatorial cosputtering (figure 4) in 2015 [37, 62]. Similar combinatorial RF sputter deposited ZTN papers continue to be published, which report changes in different physical properties as a function of Zn-Sn off-stoichiometry [63–67]. Epitaxially grown ZTN thin films on YSZ(111) substrates were RF sputter deposited from a stoichiometric Zn-Sn target[68], with a detailed analysis of optical absorption of unintentionally oxygen-doped ZTN thin film epi-layers, and of carrier scattering by neutral impurities [69]. A very recent study utilized a combined RF/DC magnetron sputter method and reported carrier mobility above 22 $cm^2\ V^{-1}\ s^{-1}$ with n-type carrier concentration below $10^{17}\ cm^{-3}$ [70], hypothesizing enhanced decomposition of N_2 molecules into activated nitrogen atoms. RF-free DC magnetron sputtering has been used by a single research group thus far [71] to grow ZTN and fabricate functioning ZTN solar cells.

As for other growth techniques, PVLS was also used to synthesize polycrystalline (pX) ZTN, and the available range of growth conditions were identified [53, 54]. The bandgap measured by photoluminescence (PL) was 1.7 eV and wurtzite-like structure was reported from XRD data. More recently, ZTN pX bulk samples were synthesized by high-pressure metathesis reaction [72], and an optical bandgap of 1.4 eV was measured. However, in a follow-up study, a bandgap of near 1.0 eV was reported for the disordered wurtzite structure [73]. There has not been any report of Chemical Vapor Deposition (CVD) growth of ZTN thus far, however $ZnGeN_2$ and $ZnSiN_2$ growth by MOCVD has been reported [74]. Since several different Sn containing CVD precursors exist, ZTN growth by CVD (likely, plasma assisted) may be possible too.

An important observation across the experimental studies is the wide variance of the measured electrical properties and optical bandgaps (table 1), with values ranging for carrier concentration 10^{16}–$10^{21}\ cm^{-3}$, for electron mobility 0.5–22.7 $cm^2\ V^{-1}\ s^{-1}$, and for optical bandgap 1.0–2.4 eV. This is due to the fact that crystal structure, defect density, Zn-Sn stoichiometry, and oxygen level all play a part in determining the bandgap and charge transport properties. In particular, local disorder, which may [75], or may not [65] be detectable from the conventional XRD measurement, directly impacts the optical bandgap [44]. In addition, ZTN can be an n-type degenerate semiconductor, so the carrier concentration may also shift the measured optical bandgap due to Burstein-Moss filling of the bands. The level of intentional or unintentional oxygen incorporation and its effect on bandgap only came into attention in very recent literature [48]. All these parameters often remain under-reported in literature, so care should be taken by the scientific community in interpreting the past literature and future publications.

2.3. Device fabrication and modeling

Despite enormous potential for device applications, to date only one research group reported PV device fabrication with ZTN deposited using DC magnetron sputtering. For initial devices, ZTN was deposited on p-Si substrates, with Zn-rich off-stoichiometric film of $\sim 10^{17}\ cm^{-3}$ electron concentration [77]. Current-voltage rectification was demonstrated with this p-Si/n-ZTN heterojunction diode structure. In two follow up publications, p-SnO/n-ZTN solar cells were reported, with n-ZTN prepared using DC magnetron sputtering [78]. The reported photo conversion efficiency was improved up to 1.54% by using an Al_2O_3 buffer layer [38], with the reported J-V data shown in figure 5.

In addition to these experimental reports, the prospect of PV device fabrication based on ZTN absorber was also investigated by modeling [79]. Simulated device performance of a ZTN/Mg:$CuCrO_2$ solar cell, indicated a possible efficiency of 23% in the ideal case of no defects present. Furthermore, various performance-limiting real-world criteria, such as presence of band tails in ZTN, minority carrier mobility, defect levels/recombination centers and band alignment with p-TCO, were investigated and their impact on PV device performance was projected. The importance of maximizing hole mobility was highlighted in this modeling work, since a high hole mobility was shown to have a significant positive effect on several performance parameters even in the presence of band tails or recombination center defects.

3. Highlights from $ZnSnN_2$ materials research at NREL

In this section, we highlight several research accomplishments on $ZnSnN_2$ material at the National Renewable Energy Laboratory (NREL) which has enabled a better understanding of its structure and properties by the scientific community.

Table 1. Reported properties of $ZnSnN_2$, in both theoretical and experimental publications.

Year of Publication	Method	Bandgap (eV)	Electron Concentration (cm^{-3})	Electron Mobility ($cm^2 V^{-1} s^{-1}$)	References
2009	Computations—LDA	0.7	—	—	[39]
2011	Computations—LDA, GGA	2.02	—	—	[41, 42]
2012	Experiments—MBE	2.0	—	—	[76]
2013	Computations—LDA, QSGW	1.8	—	—	[43]
2013	Computations—PBE0, Experiments—MBE	1.12–2.09, 2.12–2.38	$3x10^{20}$–$1x10^{21}$	10	[52]
2013	Computations—Plasma VLS	1.7		—	[53]
2013	Experiments—RF Sputtering	2.0	$5x10^{19}$–$1x10^{21}$	$\leqslant$10	[51]
2015	Experiments—RF Sputtering	1.0–1.4	$2x10^{18}$–$2x10^{20}$	1.1–8.3	[37]
2015	Experiments—DC Sputtering	1.9	$2x10^{17}$–$2x10^{18}$	1.86–3.98	[71]
2016	Experiments—Metathesis	1.4	—	—	[72]
2017	Experiments—RF Sputtering	~1.0	$4x10^{16}$–$2x10^{18}$	0.5–8.8	[62]
2017	Computations—Monte Carlo	0.8–1.4	—	—	[47]
2018	Experiments—RF Sputtering	1.8	$1x10^{19}$	3.8	[60]
2018	Experiments—RF Sputtering	1.67	$9.58x10^{17}$	3.79	[38]
2019	Computations—Monte Carlo	1.4–1.9	10^{17}–10^{20}	—	[48]
2019	Experiments—Plasma MBE	1.6–2.0	$6x10^{18}$–$3x10^{20}$	9.8–22.5	[58]
2020	Experiments—Sputtering	1.43	$9.92x10^{16}$	22.7	[70]

LDA—Local Density Approximation, GGA—Generalized Gradient Approximation, PBE—Perdew-Burke- Ernzerhof gradient corrected functional, QSGW—self-consistent GW approximation

3.1. Monte Carlo simulations of disorder in stoichiometric ZTN [47]

Early literature on computational predictions of disorder in $ZnSnN_2$ considered only one of the two extreme limits: fully randomized cation disorder [52], or a minimum level of disorder maintaining the local octet rule [42, 44]. However, due to electrostatic interactions in heterovalent systems (here Zn^{2+} and Sn^{4+}), significant short-range order effects would be expected between these two limits. To bridge the gap between these two limits of disorder, a motif-based model Hamiltonian was used for Monte Carlo simulations with a 128-atom supercell for varying degrees of disorder. The model Hamiltonian motifs were centered on the N anion, and expanded the energy out to $\Delta H = 2\sum_{i,j} e_{i,j}n_{i,j}$, in which $n_{i,j}$ counts the number of N-Zn_iSn_j motifs, and e is the energy of the motif, calculated using a least-squares fit to DFT energies with randomly distributed cations and equal numbers of Zn and Sn.

The effective temperature of the simulation started at 3500 °C and was cooled at a rate of 10^4 K^{-1} to give a measure of disorder resulting from non-equilibrium growth. A transition from the octet-rule conserving Zn_2Sn_2 motif to introduction of more Zn_3Sn_1 and Zn_1Sn_3 motifs at around $T_{eff} = 2000$ °C was observed, as shown in figure 6(a). Given that sputtering is a common synthesis technique used for ZTN grown, this effective temperature is feasible in experimental synthesis due to the high energy, non-equilibrium nature of this growth technique. The amount of 31 and 13 motifs can be used as a descriptor for cation disorder of the stoichiometric $ZnSnN_2$. Toward higher effective temperatures, the amount Zn_3Sn_1 and Zn_1Sn_3 motifs in the model leveled out at around 0.2, rather than continuing along the initial exponential increase trend. With an increasing level of disorder, exchange defects could not form independently and are subject to constraints. The energetically unfavorable Zn_4 and Sn_4 motifs did not show up in appreciable amounts at any effective temperature. This leveling out of the motif fractions showed an effective phase transition resulting from the effects of configurational entropy.

Comparing measured XRD of a stoichiometric $ZnSnN_2$ film to simulated XRD for supercells with varying degrees and types of disorder (e.g. octet-rule conserving vs. fully random cation distribution) showed a lack of the cation ordering present in the experimental sample. However, even a moderate degree of octet-rule violating disorder would lead to patterns indistinguishable from the fully randomized structure, due to insensitivity in the XRD patterns to further increasing levels of disorder. The lattice parameters of the wurtzite structure and the orthorhombic cation-ordered structure are very similar, further impeding structure identification of the experimental results via XRD.

The magnitude of the bandgap of ordered orthorhombic $ZnSnN_2$ had not been well established, and experimental measurements gave values anywhere between 1 and 2 eV. Note that the variation in these literature values was in part due to Burstein-Moss filling of the bands, which is discussed further in this article. To calculate the electronic structure as a function of disorder, a parameterized single-shot hybrid + U (SSH + U) function was used, keeping the DFT + U wave functions fixed to avoid the computational

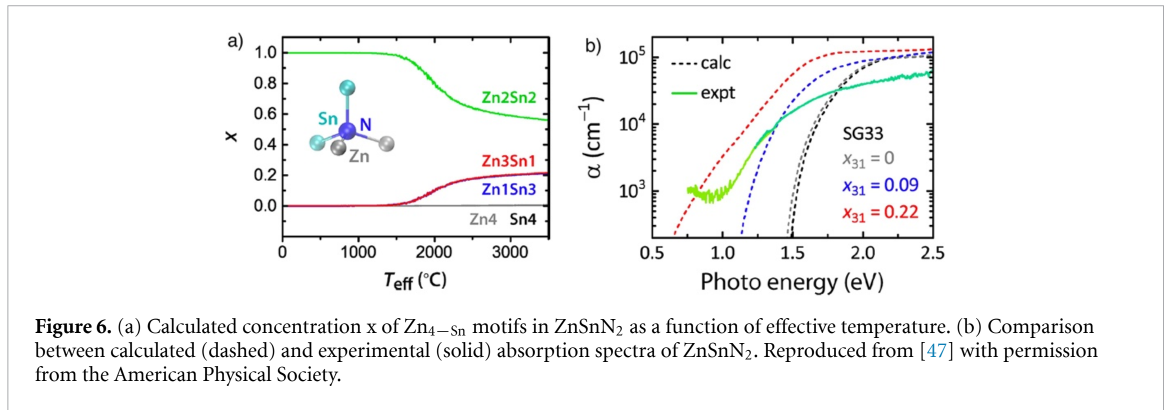

Figure 6. (a) Calculated concentration x of Zn_{4-Sn} motifs in $ZnSnN_2$ as a function of effective temperature. (b) Comparison between calculated (dashed) and experimental (solid) absorption spectra of $ZnSnN_2$. Reproduced from [47] with permission from the American Physical Society.

complexity of having to diagonalize the hybrid functional Hamiltonian each time. From these calculations, the absorption spectra were calculated for the fully ordered, octet-rule conserving disordered, and for varying degrees of 31 disordered stoichiometric structures. Introducing disorder but conserving the octet rule resulted in only minimal reduction of the bandgap by around 0.02 eV, while a band-gap reduction of 0.3–0.4 eV for intermediate levels of disorder around $X_{31} = 0.1$ was shown to be plausible, as shown in figure 6(b). The bandgap was calculated at 1.5 eV in the ordered orthorhombic state, and to approach 1 eV with increased levels of disorder characterized by increasing 31 and 13 motifs.

Disorder also had an effect on the inverse participation ratio (IPR) near the band edges, which measures the inverse fraction of atoms contributing to the density of states (DOS). The IPR effectively gives a measure of the localization of the electronic density of states, where IPR = 1 is complete delocalization, and IPR = 10 implies the state is localized on average of one out of ten atoms. Moderate localization effects occurred around the valence-band maximum for the formation of Zn_3Sn_1 and Zn_1Sn_3, but the conduction band remained essentially unperturbed for these conditions. Full randomization resulted in a continuum of defect states throughout the band-gap region, confirming the closing of the gap for highly disordered $ZnSnN_2$.

3.2. Doping tuning by off-stoichiometry and transport properties [37]

Experimental exploration of ZTN at NREL [37] involved combinatorial RF sputter deposition from Zn and Sn targets with an activated N_2 source (figure 4). With PV and photoelectrochemical (PEC) device applications as the long term vision, the goal was to lower carrier concentration for this degenerate n-type semiconductor while maintaining sufficiently high mobility. Zn/Sn off-stoichiometry along with variations in deposition temperature were explored to study the cation disorder and phase stability as a function of growth conditions and composition.

Figure 7 represents the summary of deposition temperature and stoichiometry space explored via combinatorial experiments. ZTN thin films were deposited on glass substrates with orthogonal Zn-to-Sn gradients in cation composition between 0.30 and 0.75 Zn/(Zn + Sn) and growth temperatures ranging from 35 to 340 °C. Films grown in the temperature range from 160 to 340 °C with cation compositions from 0.45–0.70 Zn/(Zn + Sn) exhibited the typical wurtzite crystal structure, with no signs of secondary phase formation. Temperatures over 350 °C were found to be non-optimal, with no net deposition or deposition of metallic Zn and Sn. The absence of secondary phases over variable growth conditions and wide range of Zn off-stoichiometry might be in part due to the use of an activated N source, but there could be other factors as well. Single point TEM analysis confirmed polycrystalline film morphology, with some preferential orientation (texturing) along the c-axis (0001) direction. No metallic Zn or Sn precipitates were observed in electron backscatter diffraction (EBSD) grain orientation maps for stoichiometric or 0.55 Zn/(Zn + Sn) films. However, small regions of high dislocation density and nano-scale voids were observed within grain interiors from HAADF and HRTEM.

The cation-ordered orthorhombic ZTN structure has a predicted bandgap of around 1.5 eV, while the cation-disordered wurtzite-derived structure approaches 1 eV [47]. As the cation composition of Zn decreases from 0.60 to 0.40 Zn/(Zn + Sn), the following trends are observed: (i) absorption onset increased from 1.0 to 1.4 eV, (ii) more free carrier absorption was observed, as shown by the increase in absorption coefficient at low photon energies preceding the absorption edge, and (iii) carrier concentration increased. These trends suggest that a Burstein-Moss shift was responsible for increasing the apparent bandgap for films with lower Zn content. Curve fitting of the absorption edge vs. carrier density plot revealed an effective mass of $m^* = 0.5\ m_e$. PL was observed as a broad peak at 1.35–1.5 eV, which was further investigated in later research.

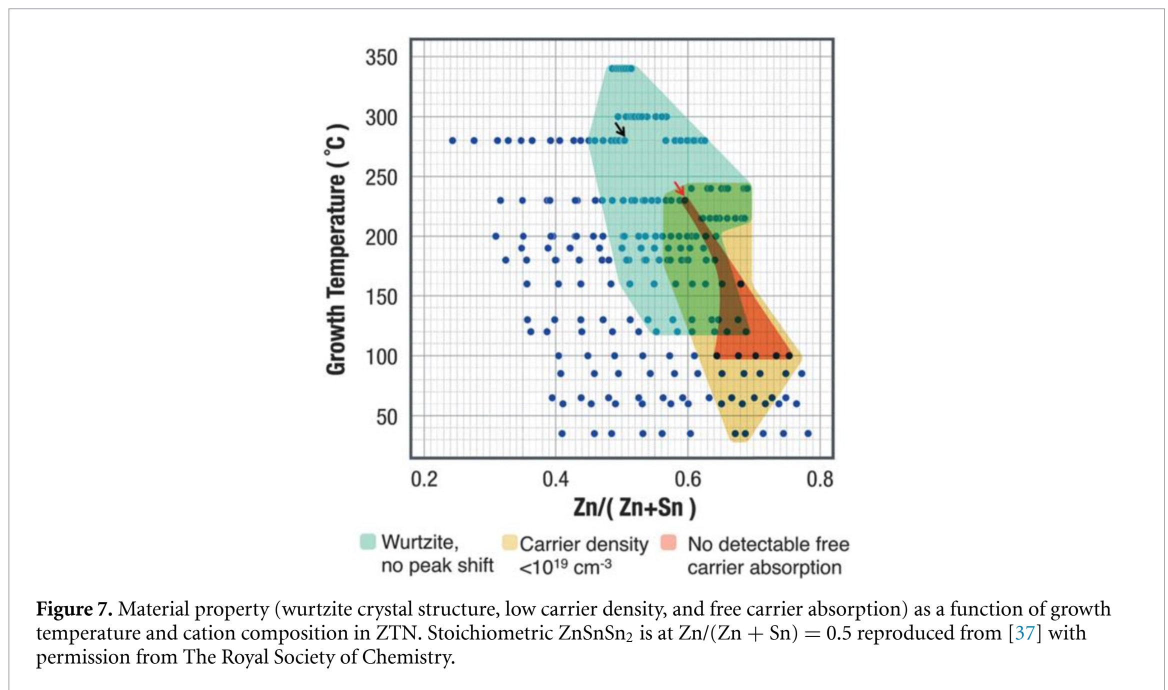

Figure 7. Material property (wurtzite crystal structure, low carrier density, and free carrier absorption) as a function of growth temperature and cation composition in ZTN. Stoichiometric $ZnSnSn_2$ is at Zn/(Zn + Sn) = 0.5 reproduced from [37] with permission from The Royal Society of Chemistry.

Conductivity varied over four orders of magnitude as a function of cation composition and growth temperature, with a minimum conductivity occurring at around Zn/(Zn + Sn) = 0.65. This point also corresponded to a minimum in free electron density, decreasing by more than 2 orders of magnitude with the same trends as the conductivity. The lowest n-type carrier density was 1.8×10^{18} cm^{-3} for film grown at 230 °C with Zn/(Zn + Sn) of 0.70. This carrier density was 2 orders of magnitude lower than what was previously reported [51]. Zn off-stoichiometry aided in the reduction in carriers, likely through compensation of O_N and V_N defects (both low energy defects in $ZnSnN_2$) via excess Zn on the disordered cation sublattice compensating these anion defects.

Carrier mobility ranged from 1.1 to 8.3 cm^2 V^{-1} s^{-1}, with no clear trend across temperature or composition. The inverse relationship between carrier density and mobility as a function of cation stoichiometry suggested the loss of charge scattering centers with increasing Zn content. This could be due to the formation of defect complexes with increasing Zn content. Rutherford Backscattering Spectroscopy (RBS) on a nominally stoichiometric sample showed around 4% O incorporation, further substantiating the possible effect of defect complexes involving the O_N and V_N defects. For stoichiometric and 0.6 Zn/(Zn + Sn) films, no temperature dependence of carrier concentration and mobility was observed.

3.3. Doping control by incorporation and removal of hydrogen [62]

Following in the footsteps of GaN p-type doping control [81], continuation of this experimental study of ZTN deposition [62] involved changing the ambient gases present during the deposition, and incorporation of a post-deposition annealing step. Based on the findings from the previous study, the films were deposited at 200 °C in forming gas (5% H_2/balance N_2), via RF sputtering with N_2 plasma. The anneal was performed at 400 °C for 6 h with activated N_2 ambient. ZTN films grown with forming gas, followed by annealing in N_2 exhibited a decreased n-type carrier density down to 4×10^{16} cm^{-3} for Zn-rich films (Zn/(Zn + Sn) = 0.68), as shown in figure 8. This was a significant achievement, since this carrier concentration is low enough for use as a PV light absorber layer. However, electron mobility consistently decreased from 5–8 cm^2 V^{-1} s^{-1} to less than 1 cm^2 V^{-1} s^{-1} upon annealing, possibly due to an increase in the activated acceptor density, leading to increased ionized point defect scattering.

SIMS measurements on films grown in forming gas revealed twice as much H in the as-deposited films compared to the annealed films. Changes in carrier concentration can be explained by the change in hydrogen content from a point defect perspective: (i) For Zn-rich films, Zn_{Sn} anti-site acceptor defects compensated the donor-like nitrogen vacancies V_N and O_N unintentional impurities. (ii) H atoms could form complexes w/excess Zn atoms, rendering them electrically neutral. Formation energy of donor defects is a function of Fermi energy level, and the lower concentration of active acceptor defects could lower the driving force to form additional donor defects. (iii) Zn-H complexes dissociated during annealing, re-activating the Zn_{Sn} acceptors, and compensating O_N and V_N donor defects. Assuming 4% overall oxygen

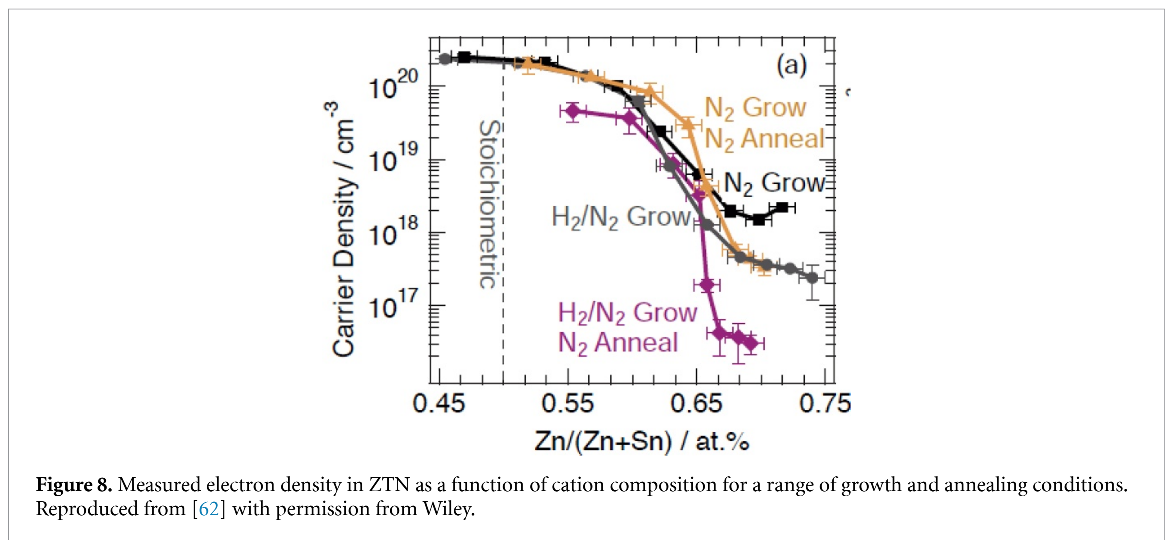

Figure 8. Measured electron density in ZTN as a function of cation composition for a range of growth and annealing conditions. Reproduced from [62] with permission from Wiley.

defects and singly ionized V_N defects, this suggested an anion concentration of 3.5% V_N defects, similar to the 2.5% value from previous results.

3.4. Exciton PL and defect complexes in ZTN [80]

A more focused investigation into the electronic quality and defect interactions of Zn-rich ZTN films is presented in [80]. The thin film deposition scheme remained identical to previous reports, including selected samples with post-deposition annealing. Characterization of the films was performed via high-resolution x-ray diffraction (HRXRD), XRF and PL. Certain experimentally characterized properties of ZTN thin films, such as a reduced carrier concentration at Zn-rich off-stoichiometry, could not be fully explained with the defect model available. Based on the measured oxygen content of these films, this study modeled the material as an alloy between ZTN and ZnO for Zn-rich films to better explain the characterization data.

The a-parameter of the lattice was found using Pawley refinement of the HRXRD data for films deposited in nitrogen and forming gas without annealing, and in forming gas with annealing. The a-parameter decreased linearly with increasing Zn content in all three samples up to a threshold. For the films grown in forming gas, the a-parameter was offset to larger values compared to the N_2-grown library, which may be due to hydrogen incorporation in the lattice. This theory is supported by SIMS measurement from previous work.

Vegard's law was applied to the observed linear lattice parameter shifts, which then suggests successful mixing in the alloy between ZTN and ZnO. This would necessitate oxygen impurity incorporation onto the nitrogen lattice sites as oxygen substitutional defects (O_N). Based on this alloy hypothesis, Monte Carlo (MC) simulations were performed for off-stoichiometric $Zn_{1+x}Sn_{1-x}(N_{1-x}O_x)_2$. Effective temperature acts as a measure of disorder present in the film, and during annealing the disorder is reduced, so the T_{eff} approached the physical annealing temperature in the experiments. Consistency between the lattice parameters calculated and in the experimentally deposited films allows for two conclusions to be drawn: (1) excess Zn occupies the cation sites rather than forming a secondary phase, and (2) oxygen incorporation encourages formation of the Zn-rich structure, supporting the ZTN/ZnO alloy hypothesis.

The Zn-rich films were found to exhibit only near-band-edge PL from excitons, shallow donors, and acceptors. This confirmed the high electronic quality and helps explain the incongruity with off-stoichiometry and structural disorder via defect formation energy calculations. Low temperature PL taken at 4.25 K showed a broad PL emission peak near 1.42 eV for both annealed and unannealed films, as shown in figure 9, which is attributed to band-edge recombination. For annealed films, a sharper peak occurred at 1.48–1.50 eV, which did not show up in the as-deposited films. This high-energy peak was assigned to bound excitons in the annealed films.

Power and temperature dependent PL emission spectra were taken for the annealed Zn-rich sample to determine the origin of the PL emission peaks. With increasing excitation laser power, the 1.49 eV peak position did not shift, while the 1.42 peak exhibited a blue-shift of 25 meV per decade. As temperature was increased, the 1.49 eV peak intensity decreased until it quenched out at 90 K. Applying the Varshni equation to the 1.49 eV peak to determine the temperature-dependent bandgap changes in the high-energy PL peak shift resulted in Varshni parameters intermediate to the values for GaN and InN, and the temperature dependence was determined to be 0.2 meV K^{-1}, or 60 meV over the range of 0–300 K. The 1.42 eV PL peak for the films cannot be explained using the donor-acceptor pair (DAP) recombination model and may be

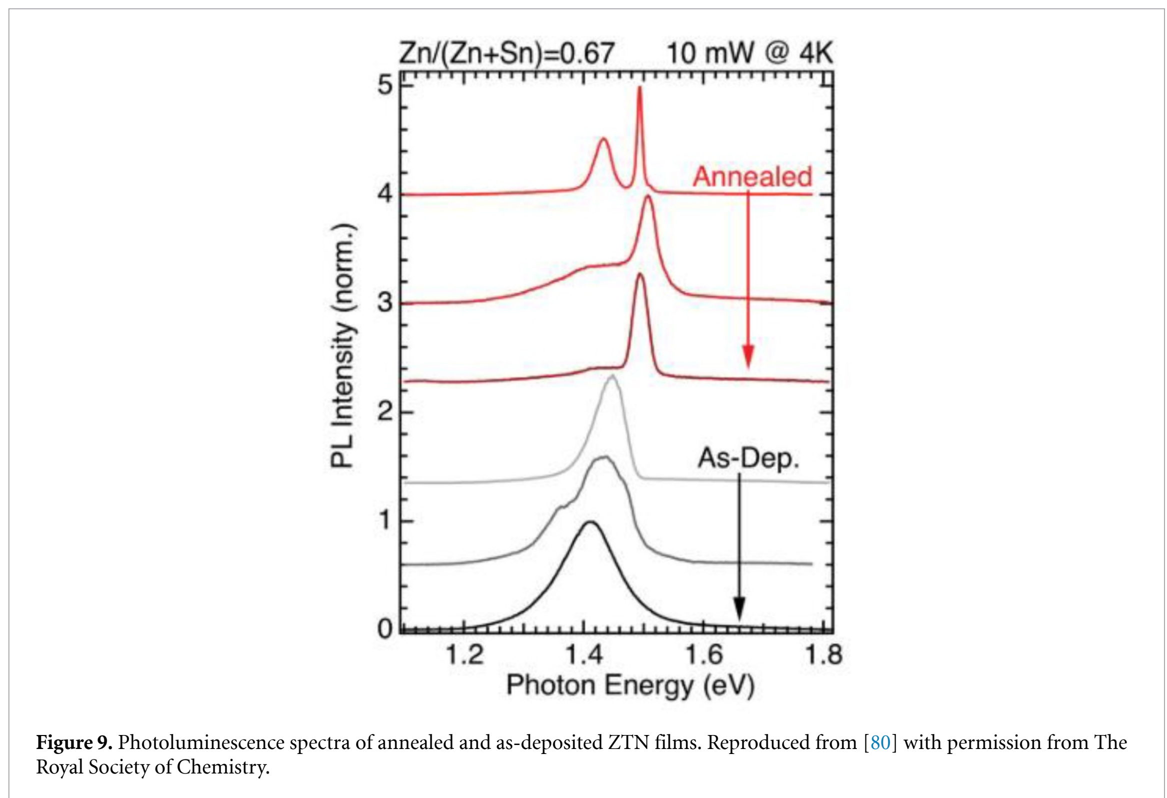

Figure 9. Photoluminescence spectra of annealed and as-deposited ZTN films. Reproduced from [80] with permission from The Royal Society of Chemistry.

due to electrostatic potential fluctuations at the band edges or bandgap variations due to variations in the cation disorder after annealing.

The exciton peak was only observed for annealed ZTN films, suggesting that the annealing step modifies the electronic structure to enhance exciton emission. Calculations for the defects were performed using a nitrogen chemical potential of $\Delta\mu N = +0.5\,eV$, which is positive to account for the activated nitrogen source. From these calculations, the formation energy of Zn_{Sn} acceptor for n-type ZTN decreases as it complexes with more O_N donors. The bandgap was found to widen as the effective temperature decreased in the MC runs, corresponding to decreased non-equilibrium disorder created by the annealing step. Since $(Zn_{Sn} + 2O_N)$ is a neutral defect pair, it is rendered electronically benign, effectively reducing the density of defect states in the bandgap. This increases the electronic quality and allows for the observed exciton luminescence despite structural disorder.

3.5. Temperature dependent Hall measurements [82]

O-containing ZTN (ZTNO) exhibits attractive properties such as a lower carrier concentration and near band edge photoluminescence, which is explained in earlier experimental and computational studies [80] based on a ZTN/ZnO solid solution model. This study aimed to experimentally validate this defect model by performing temperature-dependent Hall effect measurements on polycrystalline ZTNO thin films prepared by RF sputtering. The studied films were of Zn-rich off-stoichiometry with increasing Zn content, corresponding to increased concentration of oxygen impurities. The deposition procedure was identical to the films of [80]. The oxygen content of the films was quantified by SIMS measurement calibrated with RBS data. A cation ratio of $O/(O + N) = 0.28$ was measured for the sample with $Zn/(Zn + Sn) = 0.65$, with a decreasing level of oxygen incorporation with decreasing Zn content.

Temperature dependence of the carrier concentration was mostly flat, indicating the absence of deep donors and acceptors. The carrier mobility was also observed to be temperature independent for the near-stoichiometric degenerate samples. With increasing Zn composition, the samples turned non-degenerate, carrier mobility increased became more temperature dependent.

Temperature-dependent carrier mobility for the non-degenerate $ZnSnN_2$ samples was fitted with a mobility model based on possible scattering mechanisms of neutral defects, ionized impurities, and grain boundaries (GB). The concentrations of those defects and the effective potential barrier due to GB was calculated from the model, as shown in figure 10. Several orders of magnitude higher concentrations for the ionized donors-acceptors and also the neutral defects, compared to the carrier concentration, validate the notion that ZTNO is a heavily compensated material. Inclusion of neutral defects was essential to the accuracy of the model. First principles computational modeling data of ZTNO was used to complement the

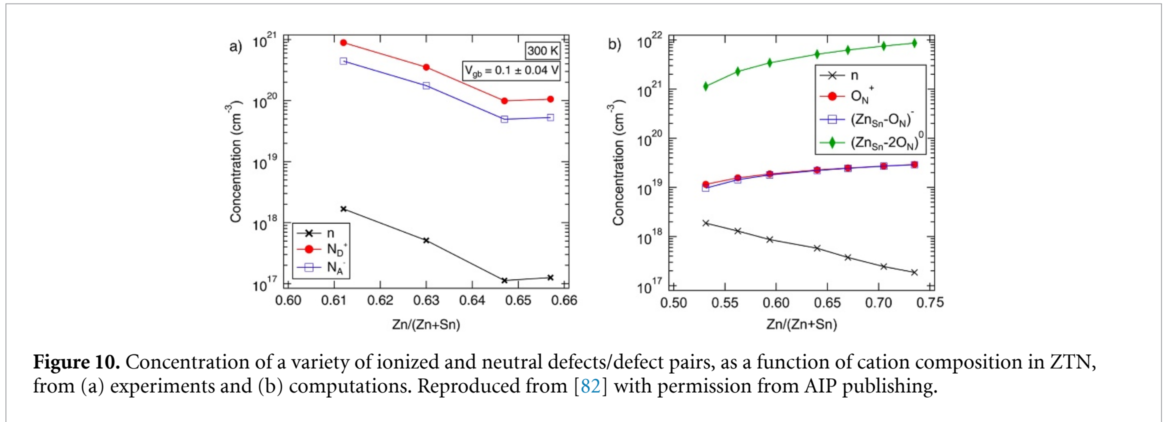

Figure 10. Concentration of a variety of ionized and neutral defects/defect pairs, as a function of cation composition in ZTN, from (a) experiments and (b) computations. Reproduced from [82] with permission from AIP publishing.

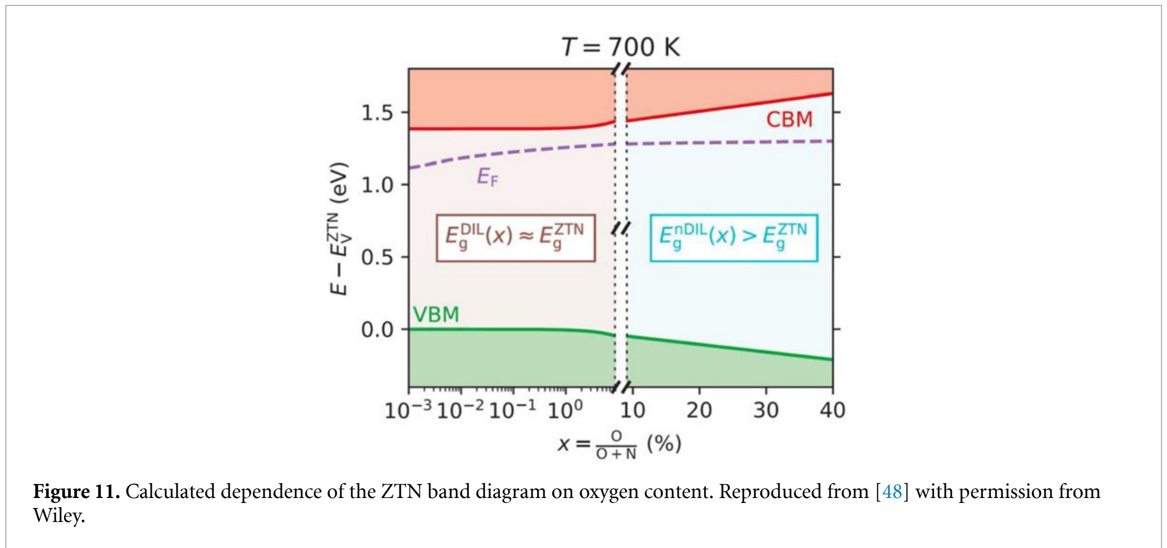

Figure 11. Calculated dependence of the ZTN band diagram on oxygen content. Reproduced from [48] with permission from Wiley.

results from mobility modelling. The neutral defects were assigned to the abundantly available $(Zn_{Sn}\text{-}2O_N)^0$ defect complexes.

3.6. Dual Sublattice mixing in $ZnSnN_2$:O [48]

Some of the most promising electronic properties for ZTN thin films have been shown to occur in oxygen-containing Zn-rich samples. Understanding the role of oxygen in ZTN introduces a level of complexity that requires more than just the typical defect models. The following need to be accounted for: (1) nonequilibrium synthesis leads to chemical potentials that can exceed equilibrium limits, (2) defects are likely to form pairs and complexes at high concentrations, (3) short range order is likely to occur, as is statistical defect pair formation, (4) the electronic band structure is altered by these defects, and (5) band edge shifts affect defect formation energies and change the defect equilibrium environment.

Continuing with the motif-based Hamiltonian approach put forth in [47], an additional level of disorder was introduced by adding oxygen to the system. Thus, the motifs were each either centered around oxygen or nitrogen atoms. Net doping depends on defect equilibrium through both the pair/cluster binding energy and the law of mass action. With dilute O compositions, the equilibrium Fermi level E_F first increased, causing n-type doping, as shown in figure 11. This trend did not continue, as at higher O concentrations, the conduction band maximum (CBM) increased, in effect decreasing the doping levels.

There is the possibility to form stable pairs of defects with opposite charge, such as O_N^{+1} and Zn_{Sn}^{2-}. Association and dissociation of the free pair defects with opposite charge to create a charge neutral group ($Zn_{Sn} + 2O_N$ pairs) is of importance in the charge balancing and doping levels. At low O levels, net doping increases due to the single-donor nature of the oxygen on the nitrogen site (+1 charge). With increasing O incorporation, most of the O_N donors are passivated by Zn_{Sn}, which effectively couples the O/N and Zn/Sn stoichiometry. This brings it closer to the ideal formula for $Zn_{1+x}Sn_{1-x}N_{2-2x}O_{2x}$, corresponding to a ZTN/ZnO solid solution. Net doping starts to decrease above 1.84 at% O.

Use of a nitrogen plasma source changes the thermodynamics of the system and assists in formation of the nonequilibrium state, since the activity of the nitrogen is increased. This introduces additional range for the chemical potentials, which expands accessibility of the phase space of ZTN. Fairly high oxygen

concentrations, along with a concomitant Zn-rich cation ratio and activated nitrogen source, is predicted to yield the lowest doping levels, even lower than those in oxygen-free ZTN. There is a trade-off between the ideal bandgap of ZTN (around 1.5 eV) and lowering the carrier concentration. ZTNO is always n-type, with carrier concentrations up to 10^{20} cm^{-3} at Sn-rich and intermediate nitrogen activities. With highly activated nitrogen, at Zn-rich conditions, electron density can be reduced to the 10^{17} cm^{-3} range according to the theoretical model.

Overall, this paper added to the computational approach by incorporating nonequilibrium, insight from growth conditions, disorder, and off-stoichiometry from impurities interacting with defects. The role that oxygen plays in ZTN electronic structure was investigated, and an explanation for the decrease in carrier concentrations with some level of oxygen incorporation was presented.

4. Summary, conclusions, and future work

As summarized in figure 2, ZTN research has come a long way in the past decade, starting from promising computational predictions in 2008 and initial successful synthesis in 2013. ZTN and other II-IV-V_2 materials have been predicted to have a wide range of optical and electronic properties, depending on composition and cation ordering. The crystal structure of ZTN, and in particular its cation disorder, has been extensively studied by different computational methods. ZTN has been synthesized in epitaxial, polycrystalline and powder forms by a wide range of bulk and thin-film deposition techniques. The optical absorption onset, photoluminescence, electron density, Hall mobility, and other relevant properties have been measured by multiple groups. Control of cation ordering and its tuning of the bandgap has been claimed, albeit with limited experimental evidence. A few reports on PV device demonstrations also exist, but there are no reports on reproducing these fabrication or measurement experiments yet.

ZTN research activities at NREL over the last few years have impacted the global research efforts in investigating this emerging material. Experimental exploration of ZTN using high throughput combinatorial RF sputtering surveyed the temperature and Zn-to-Sn ratio space for $ZnSnN_2$ deposition [37], leading to significant reduction of unintentional doping. The results of the experimental studies were complemented by first principles calculations, which explained the character of cation disorder and allowed for predictions of the electrical and optical properties [47]. The use of forming gas during deposition and optimized post-deposition annealing resulted in the lowest reported electron concentration approaching 10^{16} cm^{-3} thus far for ZTN, with minimal reduction in carrier mobility [62], and with room-temperature near-band-edge photoluminescence [80]. The most recent computational study explained the role of oxygen in ZTN growth, highlighting that the zinc-rich oxygen-substituted material should rather be thought of as zinc tin oxy-nitride[48], and the following temperature-dependent Hall effect measurements supported these predictions [82]. The close relationship between computational and experimental work in the ZTN material system has allowed for in-depth analysis and iterative model formation, which could be the key to improving ZTN and other new materials in the next generation of PV device applications.

One of the most important findings in ZTN research was that oxygen incorporation plays a critical role in the electronic quality and defect interactions in ZTN films. Oxygen incorporation into the ZTN films was shown to be experimentally facile if not inevitable, due to a base pressure of water in the sputtering chamber rather than through intentional oxygen incorporation [37, 80]. This factor may have led to a wide range of carrier concentrations with no distinguishing factor to differentiate between the varying films (table 1). On one hand, oxygen substitution in stoichiometric $ZnSnN_2$ leads to degenerate electron density, which is detrimental to PV device applications. On the other hand, addition of Zn beyond the stoichiometric amounts to form a ZTN:ZnO alloy can be utilized to reduce carrier concentrations down to 10^{16} cm^{-3} [62], which brings the material closer to device applications in PV solar cells. Thus, more systematic reporting of the zinc to tin ratio and oxygen to nitrogen ratio in ZTN films would be important in future research.

Acknowledgments

This work was authored at the National Renewable Energy Laboratory, operated by Alliance for Sustainable Energy, LLC, for the U.S. Department of Energy (DOE) under Contract No. DE-AC36-08GO28308. K H was funded by Office of Energy Efficiency and Renewable Energy, Fuel Cells Technologies Program, as a part of HydroGEN Energy Materials Network (EMN). I K was funded by Office of Energy Efficiency and Renewable Energy, Solar Energy Technology Program, as a part of SunLaMP program. We would like to acknowledge numerous useful discussions and continued collaborations with Dr Adele Tamboli, Dr Stephan Lany, Dr Eric Toberer and their team members at NREL. The views expressed in the article do not necessarily represent the views of the DOE or the U.S. Government.

ORCID iDs

Imran S. Khan https://orcid.org/0000-0002-8483-2896

Karen N. Heinselman https://orcid.org/0000-0003-0287-3019

Andriy Zakutayev https://orcid.org/0000-0002-3054-5525

References

[1] Zakutayev A *et al* 2014 Defect tolerant semiconductors for solar energy conversion *J. Phys. Chem. Lett.* **5** 1117–25
[2] Zakutayev A 2016 Design of nitride semiconductors for solar energy conversion *J. Mater. Chem.* A **4** 6742–54
[3] Robertson J and Clark S J 2011 Limits to doping in oxides *Phys. Rev.* B **83** 075205
[4] Walukiewicz W 2001 Intrinsic limitations to the doping of wide-gap semiconductors *Phys. B: Condens. Matter.* **302–3** 123–34
[5] Sun W *et al* 2017 Thermodynamic routes to novel metastable nitrogen-rich nitrides *Chem. Mater.* **29** 6936–46
[6] Sun W *et al* 2019 A map of the inorganic ternary metal nitrides *Nat. Mater.* **18** 732–9
[7] Hoornaert T, Hua Z K and Zhang J H 2009 Hard wear-resistant coatings: a review *Advanced Tribology* eds Luo J, Meng Y, Shao T, and Zhao Q (Berlin: Springer) pp 774–9
[8] Raveh A, Zukerman I, Shneck R, Avni R and Fried I 2007 Thermal stability of nanostructured superhard coatings: a review *Surf. Coatings Technol.* **201** 6136–42
[9] Salamat A, Hector A L, Kroll P and McMillan P F 2013 Nitrogen-rich transition metal nitrides *Coord Chem. Rev.* **257** 2063–72
[10] Horvath-Bordon E *et al* 2006 High-pressure chemistry of nitride-based materials *Chem. Soc. Rev.* **35** 987–1014
[11] Wang B and Callahan M J 2006 Ammonothermal synthesis of III-nitride crystals *Cryst. Growth Des.* **6** 1227–46
[12] Richter T M M and Niewa R 2014 Chemistry of ammonothermal synthesis *Inorganics* **2** 29–78
[13] Yano M, Okamoto M, Yap Y K, Yoshimura M, Mori Y and Sasaki T 2000 Growth of nitride crystals, BN, AlN and GaN by using a Na flux *Diam. Relat. Mater.* **9** 512–5
[14] Yamane H and DiSalvo F J 2018 Sodium flux synthesis of nitrides *Prog. Solid State Chem.* **51** 27–40
[15] Caskey C M, Richards R M, Ginley D S and Zakutayev A 2014 Thin film synthesis and properties of copper nitride, a metastable semiconductor *Mater. Horiz.* **1** 424–30
[16] Caskey C M *et al* 2015 Semiconducting properties of spinel tin nitride and other IV3N4 polymorphs *J. Mater. Chem.* C **3** 1389–96
[17] Martinez A D, Fioretti A N, Toberer E S and Tamboli A C 2017 Synthesis, structure, and optoelectronic properties of II-IV-V2 materials *J. Mater. Chem.* A **5** 11418–35
[18] Morkoç H 1999 *Nitride Semiconductors and Devices* vol 32 (Berlin: Springer)
[19] Li G *et al* 2016 GaN-based light-emitting diodes on various substrates: a critical review *Rep. Prog. Phys.* **79** 056501
[20] Baliga B J 2013 Gallium nitride devices for power electronic applications *Semicond. Sci. Technol.* **28** 074011
[21] Ren F and Zolper J C 2003 *Wide Energy Bandgap Electronic Devices* (Singapore: World Scientific)
[22] Talley K R, Sherbondy R, Zakutayev A and Brennecka G L 2019 Review of high-throughput approaches to search for piezoelectric nitrides *J. Vac. Sci. Technol.* A **37** 060803
[23] Bhugra H and Piazza G ed 2017 *Piezoelectric MEMS Resonators* (Berlin: Springer)
[24] Akasaki I 2015 Nobel lecture: fascinated journeys into blue light *Rev. Mod. Phys.* **87** 1119
[25] Amano H 2015 Nobel lecture: growth of GaN on sapphire via low-temperature deposited buffer layer and realization of p -type GaN by Mg doping followed by low-energy electron beam irradiation *Rev. Mod. Phys.* **87** 1133
[26] Nakamura S 2015 Nobel lecture: background story of the invention of efficient blue InGaN light emitting diodes *Rev. Mod. Phys.* **87** 1139
[27] Aho A, Isoaho R, Tukiainen A, Gori G, Campesato R and Guina M 2018 Dilute nitride triple junction solar cells for space applications: progress towards highest AM0 efficiency *Prog. Photovoltaics Res. Appl.* **26** 740–4
[28] Sukrittanon S *et al* 2015 Enhanced conversion efficiency in wide-bandgap GaNP solar cells *Appl. Phys. Lett.* **107** 153901
[29] Huang X *et al* 2019 High-temperature polarization-free iii-nitride solar cells with self-cooling effects *ACS Photonics* **6** 2096–103
[30] Williams J J *et al* 2017 Refractory InxGa1-xN solar cells for high-temperature applications *IEEE J. Photovoltaics* **7** 1646–52
[31] Alotaibi B *et al* 2013 High efficiency photoelectrochemical water splitting and hydrogen generation using GaN nanowire photoelectrode *Nanotechnology* **24** 175401
[32] Alotaibi B, Nguyen H P T, Zhao S, Kibria M G, Fan S and Mi Z 2013 Highly stable photoelectrochemical water splitting and hydrogen generation using a double-band InGaN/GaN core/shell nanowire photoanode *Nano Lett.* **13** 4356–61
[33] Aryal K, Pantha B N, Li J, Lin J Y and Jiang H X 2010 Hydrogen generation by solar water splitting using p-InGaN photoelectrochemical cells *Appl. Phys. Lett.* **96** 052110
[34] Wadia C, Alivisatos A P and Kammen D M 2009 Materials availability expands the opportunity for large-scale photovoltaics deployment *Environ. Sci. Technol.* **43** 2072–7
[35] Shockley W and Queisser H J 1961 Detailed balance limit of efficiency of p-n junction solar cells *J. Phys. D: Appl. Phys.* **32** 510–19
[36] Chen S, Narang P, Atwater H A and Wang L-W 2014 Phase stability and defect physics of a ternary ZnSnN2 semiconductor: first principles insights *Adv. Mater.* **26** 311–15
[37] Fioretti A N *et al* 2015 Combinatorial insights into doping control and transport properties of zinc tin nitride *J. Mater. Chem.* C **3** 11017–28
[38] Javaid K *et al* 2018 Band offset engineering in ZnSnN2-based heterojunction for low-cost solar cells *ACS Photonics* **5** 2094–9
[39] Paudel T R and Lambrecht W R L 2009 First-principles calculations of elasticity, polarization-related properties, and nonlinear optical coefficients in Zn-IV- N2 compounds *Phys. Rev. B: Condens. Matter. Mater. Phys.* **79** 245205
[40] Paudel T R and Lambrecht W R L 2008 First-principles study of phonons and related ground-state properties and spectra in Zn-IV-N2 compounds *Phys. Rev. B: Condens. Matter. Mater. Phys.* **78** 115204
[41] Punya A, Paudel T R and Lambrecht W R L 2011 Electronic and lattice dynamical properties of II-IV-N2 semiconductors *Phys. Status Solidi Curr. Top. Solid State Phys.* **8** 2492–9
[42] Punya A, Lambrecht W R L and Van Schilfgaarde M 2011 Quasiparticle band structure of Zn-IV-N2 compounds *Phys. Rev. B: Condens. Matter. Mater. Phys.* **84** 165204
[43] Punya A and Lambrecht W R L 2013 Band offsets between ZnGeN2, GaN, ZnO, and ZnSnN2 and their potential impact for solar cells *Phys. Rev.* B **88** 75302

[44] Quayle P C *et al* 2015 Charge-neutral disorder and polytypes in heterovalent wurtzite-based ternary semiconductors: the importance of the octet rule *Phys. Rev.* B **91** 205207
[45] Tsunoda N, Kumagai Y, Takahashi A and Oba F 2018 Electrically benign defect behavior in zinc tin nitride revealed from first principles *Phys. Rev. Appl.* **10** 11001
[46] Wang T, Ni C and Janotti A 2017 Band alignment and p-type doping of ZnSnN2 *Phys. Rev.* B **95** 205205
[47] Lany S *et al* 2017 Monte Carlo simulations of disorder in ZnSnN2 and the effects on the electronic structure *Phys. Rev. Mater.* **1** 035401
[48] Pan J, Cordell J, Tucker G J, Tamboli A C, Zakutayev A and Lany S 2019 Interplay between composition, electronic structure, disorder, and doping due to dual sublattice mixing in nonequilibrium synthesis of ZnSnN2 : O *Adv. Mater.* **31** 1807406
[49] Fang D Q, Zhang Y and Zhang S L 2016 Band gap engineering of ZnSnN2/ZnO (001) short-period superlattices via built-in electric field *J. Phys. D: Appl. Phys.* **120** 30–33
[50] Fang D Q, Chen X, Gao P F, Zhang Y and Zhang S L 2017 Mono- and bilayer ZnSnN2 Sheets for visible-light photocatalysis: first-principles predictions *J. Phys. Chem.* C **121** 26063–8
[51] Lahourcade L, Coronel N C, Delaney K T, Shukla S K, Spaldin N A and Atwater H A 2013 Structural and optoelectronic characterization of RF sputtered ZnSnN2 *Adv. Mater.* **25** 2562–6
[52] Feldberg N *et al* 2013 Growth, disorder, and physical properties of ZnSnN2 *Appl. Phys. Lett.* **103** 42109
[53] Quayle P C, He K, Shan J and Kash K 2013 Synthesis, lattice structure, and band gap of ZnSnN2 *MRS Commun.* **3** 135–8
[54] Quayle P C, Junno G T, He K, Blanton E W, Shan J and Kash K 2017 Vapor–liquid–solid synthesis of ZnSnN2 *Phys. Status Solidi Basic Res.* **254** 1600718
[55] Veal T D *et al* 2015 Band gap dependence on cation disorder in ZnSnN2 solar absorber *Adv. Energy Mater.* **5** 1–5
[56] Feldberg N, Aldous J D, Stampe P A, Kennedy R J, Veal T D and Durbin S M 2014 Growth of ZnSnN2 by molecular beam epitaxy *J. Electron. Mater.* **43** 884–8
[57] Senabulya N *et al* 2016 Stabilization of orthorhombic phase in single-crystal ZnSnN2 films *AIP Adv.* **6** 075019
[58] Le D D, Ngo T S and Hong S-K 2019 Growth of single crystal non-polar (112¯0) ZnSnN2 films on sapphire substrate *Appl. Surf. Sci.* **481** 819–24
[59] Shing A M, Tolstova Y, Lewis N S and Atwater H A 2017 Effects of surface condition on the work function and valence-band position of ZnSnN2 *Appl. Phys. A: Mater. Sci. Process.* **123** 735
[60] Alnjiman F *et al* 2018 Chemical environment and functional properties of highly crystalline ZnSnN2 thin films deposited by reactive sputtering at room temperature *Sol. Energy Mater. Sol. Cells* **182** 30–36
[61] Kuo C-H and Chang K-S 2017 Piezotronic and piezophototronic properties of orthorhombic ZnSnN2 fabricated using Zn-Sn3N4 composition spreads through combinator *Cryst. Growth Des.* **17** 4694–702
[62] Fioretti A N *et al* 2017 Effects of hydrogen on acceptor activation in ternary nitride semiconductors *Adv. Electron. Mater.* **3** 3–7
[63] Cai X-M *et al* 2019 Fabricating ZnSnN2 with cosputtering *Surf. Coatings Technol.* **359** 169–74
[64] Cai X-M *et al* 2019 Tuning the photoluminescence, conduction mechanism and scattering mechanism of ZnSnN2 *J. Alloys Compd.* **779** 237–43
[65] Wu X *et al* 2019 Carrier tuning in ZnSnN2 by forming amorphous and microcrystalline phases *Inorg. Chem.* **58** 8480–5
[66] Chinnakutti K K, Panneerselvam V and Salammal S T 2019 Tailoring optoelectronic properties of earth abundant ZnSnN2 by combinatorial RF magnetron sputtering *J. Alloys Compd.* **772** 348–58
[67] Wang Y, Ohsawa T, Meng X, Alnjiman F, Pierson J-F and Ohashi N 2019 Suppressing the carrier concentration of zinc tin nitride thin films by excess zinc content and low temperature growth *Appl. Phys. Lett.* **115** 232104
[68] Cao X, Kawamura F, Ninomiya Y, Taniguchi T and Yamada N 2017 Conduction-band effective mass and bandgap of ZnSnN2 earth-abundant solar absorber *Sci. Rep.* **7** 14987
[69] Cao X, Kawamura F, Taniguchi T and Yamada N 2020 Electron transport properties of degenerate—ZnSnN 2 doped with oxygen *BMC Mater.* **2** 4
[70] Ye F *et al* 2020 Improving the chemical potential of nitrogen to tune the electron density and mobility of ZnSnN2 *J. Mater. Chem.* C
[71] Deng F *et al* 2015 Determination of the basic optical parameters of ZnSnN2 *Opt. Lett.* **40** 1282
[72] Kawamura F, Yamada N, Imai M and Taniguchi T 2016 Synthesis of ZnSnN2 crystals via a high-pressure metathesis reaction *Cryst. Res. Technol.* **51** 220–4
[73] Kawamura F, Yamada N, Cao X, Imai M and Taniguchi T 2019 The bandgap of ZnSnN2 with a disordered-wurtzite structure *Jpn. J. Appl. Phys.* **58** SC1034
[74] Muth J, Cai A, Osinsky A, Everitt H, Cook B and Avrutsky I 2005 Optical properties of II-IV-N2 semiconductors *Materials Research Society Symp. Proc.* **831** 745–9
[75] Makin R A *et al* 2019 Alloy-free band gap tuning across the visible spectrum *Phys. Rev. Lett.* **122** 256403
[76] Feldberg N *et al* 2012 ZnSnN2: a new earth-abundant element semiconductor for solar cells *Conf. Record of the IEEE Photovoltaic Specialists Conf.* pp 2524–7
[77] Qin R *et al* 2016 Semiconducting ZnSnN2 thin films for Si/ZnSnN2 p-n junctions *Appl. Phys. Lett.* **108** 142104
[78] Javaid K *et al* 2018 Thin film solar cell based on ZnSnN2/SnO Heterojunction *Phys. Status Solidi Rapid Res. Lett.* **12** 1700332
[79] Arca E *et al* 2018 Band edge positions and their impact on the simulated device performance of ZnSnN2-based solar cells *IEEE J. Photovoltaics* **8** 110–17
[80] Fioretti A N *et al* 2018 Exciton photoluminescence and benign defect complex formation in zinc tin nitride *Mater. Horiz.* **5** 823–30
[81] Neugebauer J and Van De Walle C G 1995 Hydrogen in GaN: novel aspects of a common impurity *Phys. Rev. Lett.* **75** 4452–5
[82] Hamilton D C *et al* 2019 Electron scattering mechanisms in polycrystalline sputtered zinc tin oxynitride thin films *J. Phys. D: Appl. Phys.* **126** 035701